applied sciences

MDPI

Article

Inductive Imaging of the Concealed Defects with Radio-Frequency Atomic Magnetometers

P. Bevington [1,2], R. Gartman [1] and W. Chalupczak [1,*]

[1] National Physical Laboratory, Hampton Road, Teddington TW11 0LW, UK; Patrick.Bevington@npl.co.uk (P.B.); Rafal.Gartman@npl.co.uk (R.G.)
[2] Department of Physics, University of Strathclyde, Glasgow G4 0NG, UK
* Correspondence: witold.chalupczak@npl.co.uk

Received: 19 August 2020; Accepted: 28 September 2020; Published: 30 September 2020

Abstract: We explore the capabilities of the radio-frequency atomic magnetometers in the non-destructive detection of concealed defects. We present results from the systematic magnetic inductive measurement of various defect types in an electrically conductive object at different rf field frequencies (0.4–12 kHz) that indicate the presence of an optimum operational frequency of the sensor. The optimum in the frequency dependence of the amplitude/phase contrast for defects under a 0.5–1.5 mm conductive barrier was observed within the 1–2 kHz frequency range. The experiments are performed in the self-compensated configuration that automatically removes the background signal created by the rf field producing object response.

Keywords: non-destructive testing; magnetic induction tomography; atomic magnetometer

1. Introduction

The non-destructive testing (NDT) toolkit covers a wide range of sensing technologies including thermal [1,2], infra-red imaging [3], and ultrasound [4]. Like X-ray scans [5], inductive methods are a well established non-contact measurement technique. The generic scheme of magnetic induction tomography (MIT) includes a radio-frequency (rf) magnetic field (primary field) that creates a response (secondary field) within the object through inductive coupling with an electrically conductive and/or magnetically permeable object [6]. Specifically, in electrically conductive objects, the method relies on the generation of eddy currents by an oscillating magnetic field, i.e., the primary field, in the object of interest and on the detection of the magnetic field produced by those eddy currents, i.e., the secondary field. Asymmetries in eddy current flow caused by the presence of a defect (e.g., cracks, contamination, and corrosion) are mapped onto the amplitude and the direction of the secondary field. Hence, the amplitude and phase of the secondary field will contain a signature of any defect that is present in the object. The rf magnetic fields have a frequency dependent penetration depth that enables the detection of defects throughout its volume. The object response can be detected with a pick-up coil (measuring the change in coil inductance) or with a magnetic field sensor. Measurements based on pick-up coils [6–10] benefit from simple instrumentation, but suffer from a decrease in sensitivity at low frequencies since the measured signal is $\propto \frac{\delta B}{\delta t}$. In contrast, the sensitivity of magnetic sensors is constant over a wide range of operating frequencies (1 kHz–1 GHz) [11]. In particular, it enables operation at low frequencies, where the change in the penetration depth of the rf field is most significant. This category of sensors includes giant magnetoresistance (GMR) magnetometers [12–14], superconducting quantum interference devices (SQUIDs) [15,16] and atomic magnetometers [17–26].

The measurement of the secondary field with an rf atomic magnetometer relies on the monitoring of the amplitude and phase of the rf resonance signal created by the rf field as an object is moved under the rf primary field coil. Implementation of an rf atomic magnetometer as a magnetic field sensor brings

a superior field sensitivity ($\sim$ fT/$\sqrt{Hz}$) [11] and several novel functionalities to the NDT measurement process. In particular, the semi-vector mapping of the secondary field components generated by a defect was recently demonstrated in NDT measurements with an rf atomic magnetometer, although this sensor is typically regarded as scalar in nature [23,24]. The operation of a magnetometer in the so-called spin maser mode (self-generated drive for rf magnetic field) addresses the issue of the sensor's narrow bandwidth [25,26]. In this mode, spontaneous fluctuations of the atomic spins are detected, amplified, and fed back to the primary coil to create an rf primary field whose frequency self-tunes to the rf resonance frequency. Hence, the spin maser enables the operation of the sensor in a magnetically noisy environment, which is particularly important when studying magnetically permeable objects, where the object's local magnetisation shifts the rf resonance frequency during measurements. When operating with an external drive for the rf field, this problem can be partially addressed by active stabilisation of the local magnetic field in which the sensor operates. The residual changes of the resonance frequency make it necessary to record complete rf spectra, reducing the image acquisition rate [23].

Our previous studies have been focused on measuring object thinning in the form of a recess [22–26]. Analysis of the amplitude and phase images validated this method as a tool for monitoring defect (recess) depth. In all these studies, the recess has been located on the outer surface of the object. For the uncovered defect, the amplitude of the defect signature increases with frequency, which is a simple consequence of the growth of induction with rf field frequency. Most of the observations reported in [22–26] have been performed with the rf primary field frequency in a range of tens of kHz. One of the main challenges for existing NDT methods is the detection of concealed defects; e.g., defects covered by an insulating material, buried within, or located on an inner surface of the object. In the case of electrically conductive objects, the detection requires a balance between two mutually exclusive regimes of coupling between the rf field and the object—(1) strong coupling; ensures the generation of a detectable response, and (2) weak coupling; enables significant penetration of the rf field within the object. Condition (1) is dependent on the combination of the secondary field amplitude produced by defect, which is proportional to the operating frequency, and the sensitivity of the magnetometer. To be specific, the sensor sensitivity defines the detectable limit of a defect's signature. Condition (2) limits the detection of defects located at depths below the surface. Coupling strength scales with rf field frequency and the object thickness and the optimal operational frequency occurs at the balance between the two regimes.

In this paper, we evaluate the performance of an rf atomic magnetometer in various types of NDT measurement scenarios involving a concealed defect. Our main goal is to identify the optimum coupling between the rf field and the object, i.e., optimum operational frequency of the sensor, for detecting defects concealed by a conductive barrier or throughout the object's volume. The detection of objects has partially demonstrated the efficacy of NDT with an rf atomic magnetometer through conductive and ferromagnetic barriers [19]. The low operating frequency of the magnetometer enables the penetration of the rf field through the barrier. In the cited experiment, the rf primary field source and the sensor are located on opposite sides of the barrier, which might be impractical for in-the-field measurements. In contrast, we are exploring a more versatile detection geometry, Figure 1, over a frequency range where the skin depth spans the object thickness. In addition, it should be noted that studies of the sensor performance for various frequencies, rather than just a single frequency, could address the problem of operating the magnetometer at frequencies near noises in the ambient magnetic field.

The studies discussed in this paper are mainly carried out in the so-called self-compensated configuration, where the primary rf field is parallel to the bias magnetic field [24]. In this configuration, the magnetometer signal is only produced by the secondary field components orthogonal to the primary field. These investigations have been carried out with electrically conductive, non-magnetic aluminium objects: (1) to investigate the how the skin depth, which is related to eddy currents and rf field frequency, impacts the measurements of defects at different depths, and (2) since the changes in the local field detected by the atomic magnetometer are negligible.

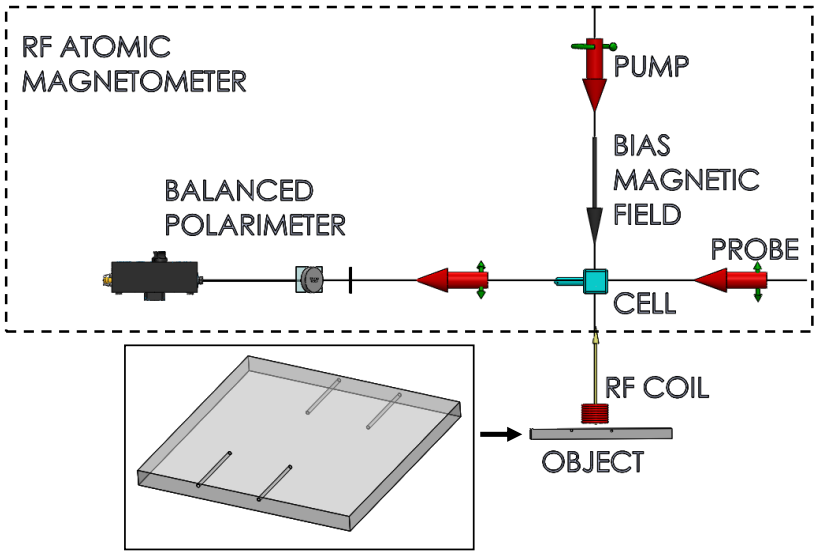

Figure 1. (colour online) Magnetic induction tomography with a radio-frequency atomic magnetometer. An rf coil produces the rf primary field that excites the object response (secondary field). The area enclosed by the dashed box shows the components that make up the rf atomic magnetometer and solid box details the geometry of the holes in the object used for the validation of concealed defect detection.

2. Experimental Setup

The measurements are performed in a magnetically unshielded environment [22–26]. The bias magnetic field is actively stabilised by three pairs of nested, orthogonal, square Helmholtz coils. The bias magnetic field amplitude sets the operating frequency of the system (i.e., the magnetic resonance frequency). Caesium atomic vapour is housed in a paraffin-coated cell at ambient temperature (atomic density $n_{Cs} = 0.33 \times 10^{11}\,\mathrm{cm}^{-3}$). Atoms are optically pumped by a circularly polarised laser beam propagating along the direction of the bias field, Figure 1. This pump beam is provided by a diode laser, frequency stabilized to the $6\,^2S_{1/2}$ F = 3$\rightarrow$ $6\,^2P_{3/2}$ F$'$ = 2 transition (D2 line, 852 nm). The evolution of the collective atomic spin is mapped through the paramagnetic Faraday effect onto the polarisation state of the linearly polarised probe beam [27–29]. The probe beam is phase-offset-locked to the pump beam, bringing it 800 MHz blue-shifted from the $6\,^2S_{1/2}$ F = 4$\rightarrow$ $6\,^2P_{3/2}$ F$'$ = 5 transition. The laser light transmitted through the cell is analysed by a polarimeter consisting of a zero-order half-wave plate, a crystal polariser and a commercial balanced photodetector. The resulting signal is measured by a lock-in amplifier referenced to the driving rf field frequency. In all the measurements, the internal rf field source of the lock-in drives the rf primary field coil. The frequency of the primary rf field is set at the operating frequency. An acoustic amplifier is added to increase the current of the lock-in rf output. The signal output of the photodetector, i.e., gain, is limited to the dynamic range of the lock-in (1 V). All the measurements rely on monitoring the response of the magnetometer while the frequency of the lock-in source is scanned through the rf resonance. The two quadrature components of the rf signal, X and Y, are recorded by the lock-in referenced to the first harmonic of the internal source (some results are expressed in terms of the amplitude $R = \sqrt{(X)^2 + (Y)^2}$ and phase $\phi = \arctan(\frac{Y}{X})$).

For aluminium objects, the rf atomic magnetometer signal (polarisation rotation caused by atomic ground state coherences) is produced by the secondary magnetic field created by eddy currents within the test object (a 150 × 150 mm^2 and 6 mm thick plate, unless stated otherwise). Eddy currents are excited by the rf coil (300 turns of 0.02 mm diameter copper, wound length of 3 mm, 2 mm and 3.5 mm inner and outer diameters). The coil has a ferrite core length 6 mm and diameter 2 mm. The coil is placed 2–7 mm from the object (coil lift-off) on the same axis as the cell and 200 mm from the atomic

magnetometer. The object is placed on a 2D translation stage actuated by two computer controlled stepper motors with 0.184 mm positioning precision.

3. Detection of the Secondary Field with an rf Atomic Magnetometer in the Self-Compensated Configuration

Use of an rf magnetometer enables the vectorial measurement of the secondary field [23]. The realisations of this idea in the so-called self-compensated configuration were demonstrated in [24]. It relies on the alignment of the rf primary and bias field such that they are both parallel to the surface normal of the studied object. Hence, the rf primary field is absent from the magnetometer signal. The observed amplitude and phase of the signal describe the components of the secondary field orthogonal to the primary field axis, i.e., the components parallel to the surface of the object. These field components are only produced in the vicinity of a defect by asymmetries in the flow of the eddy currents. Figure 2 shows the changes of the amplitude (b) and phase (c) of the rf signal over a 64 × 64 mm^2 area of a 6 mm thick aluminium plate with a single recess, whose depth changes from 0 mm to 5 mm (right to left) [23]. The red dashed line marks the position of the edge of the recess. The coil starts from a known position relative to the defects. With a known pixel/step spacing, positioning can be validated. The image was recorded in the self-compensated configuration with the atomic magnetometer operating at 1.9 kHz. It is worth pointing out that a non-zero signal is not only produced in the immediate vicinity of the recess edge, but also along the sloping area of the plate. Intuitively, this can be understood as a reflection of the rf primary field from the tilted recess surface, creating field components orthogonal to the bias field. In contrast to the phase image recorded at a higher frequency, shown in [26], the phase recorded in the vicinity of the edge [Figure 2c] contains information about the depth of the recess edge (phase changes with depth). There is a faint modulation visible in Figure 2b–f. These 'ripples' are caused by the movement of the trolley that supports the plate as it is moved by the arm of the translation stage, the ball barrings of which are slightly magnetic. The trolley only moves on one axis which accounts for the asymmetry in these ripples.

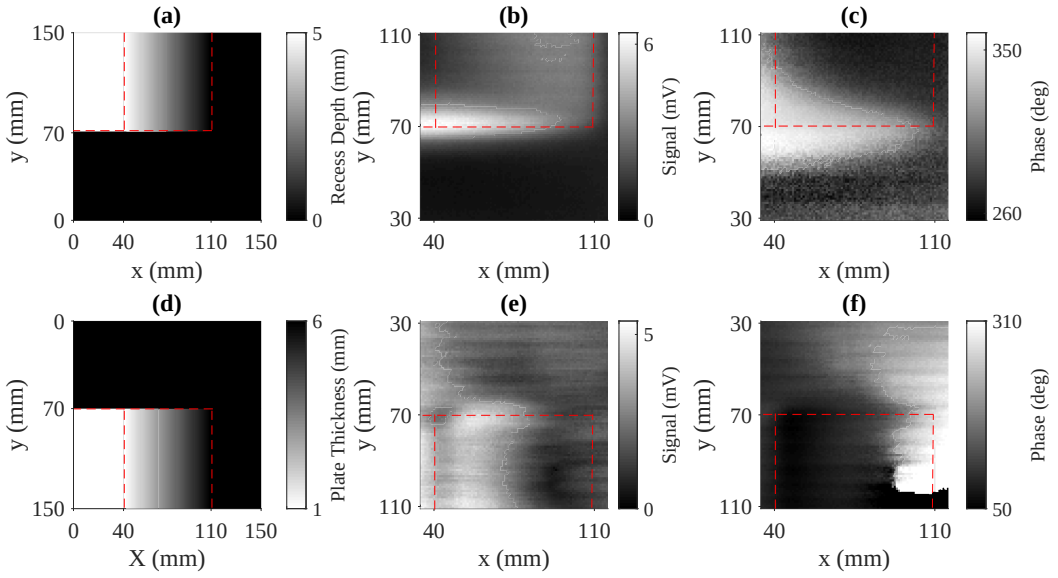

Figure 2. (colour online) The measured change of the amplitude (**b**,**e**)/phase (**c**,**f**) of the rf signal over a 64 × 64 mm^2 area of a 6 mm- thick aluminium plate with a single recess, whose depth changes from 0 mm to 5 mm (right to left). Images (**b**,**c**) are recorded with the recess on the top surface, while in (**e**), (**f**) the recessed surface is facing away from the sensor. Change of the recess depth, and inversely the plate thickness, is shown in (**a**,**d**), respectively. To record images (**b**,**c**,**e**,**f**), the same plate was simply flipped by 180°. Red dashed line marks a position of the edge of the recess.

4. Optimum Coupling between rf Primary Field and the Object

The coupling between the rf field and the electrically conductive object is characterised through the skin depth (also referred to as standard penetration depth), i.e., depth the rf field penetrates the object at which its amplitude drops to e^{-1} of its surface value. The skin depth is a function of the rf primary field frequency, electrical conductivity and magnetic permeability of the object. For skin depths larger than the thickness of the object, the coupling between the rf primary field and the object is weak; and the rf primary field is not significantly affected by propagation through the object. In the context of MIT, the object signature is imprinted in the phase of the field, while the amplitude remains relatively unchanged. An example of this case is when carrying out the inductive imaging of biological objects due to their extremely low electrical conductivity [6]. The opposite case, i.e., skin depth smaller than the object thickness, marks the regime of strong coupling. Detection of the structural defects within the objects requires significant strength of the object response (secondary field) created by the defect. For conductive objects, this translates into the optimum density of the eddy currents at a specific depth, which is a function of the operating frequency. The balance between the rf field penetration depth within the object and the minimum secondary field amplitude required raises the issue of an optimum coupling between the rf field and the object. In our studies, we tune the coupling strength by changing the operating frequency of the magnetometer, i.e., the magnetic resonance and the rf primary field frequencies, over the range of 0.45 kHz to 10 kHz.

In order to study the optimum coupling between an rf primary field and the object, we performed a series of measurements that approximate real-life defects with both simplified and more complex structures. In order to show the basic properties of the defect signature, we perform simple tests with the edge of the plate. We also discuss the influence of the overlapping signatures from opposing edges of a circular recess in a plate. Subsequently, we present the signals generated by the gradual change in the thickness of a plate, i.e., slope, rather than a sharp edge used in the previous two cases. Finally, we demonstrate measurement of the signatures of the cavities (drilled holes) at different depths that run parallel to the surface of the plate (Figure 1).

4.1. Initial Tests—Single Edge of the Plate

We begin the exploration of the topic of optimum coupling between an rf field and the object with a series of elementary measurements, recording the change in signal observed over the edge of the aluminium plate covered by thin aluminium sheets. This initial test represents the most basic structure, i.e., the signal produced by a single isolated sharp inhomogeneity under a conductive barrier with a controlled thickness. There is no other inhomogeneity in the vicinity that might affect the recorded signal, as in the case of the recess. The lift-off (distance between the primary rf field coil and the plate surface) is kept constant throughout the measurement. The measurement is performed in the self-compensated configuration.

The data shown in Figure 3 represent the measured signatures of the edge of a plate as a function of the rf primary field frequency. The measurements have been made with the edge of a 6 mm thick aluminium plate covered by zero (blue points), one (green diamonds), two (yellow triangles) and three (red squares) aluminium sheets with a thickness of 0.5 mm. There are different ways of characterising the results by considering the measured amplitude and the amplitude/phase contrast of the edge signature. The data in Figure 3a represent the frequency dependence of the amplitude of the signature of the plate edge (R), defined as $R_{\mathrm{Max}} - R_{\mathrm{Min}}$, where R_{Max} and R_{Min} are the signal amplitude measured at the opposite sides of the plate edge. For the uncovered edge, the amplitude of the signature increases with frequency, which is a simple consequence of the growth in induction with the frequency of the rf field. For the edge covered by aluminium sheets, the presence of a broad optimum in the amplitude [Figure 3a] is indicated by the shift in the slope of the frequency dependence with the number of the sheets.

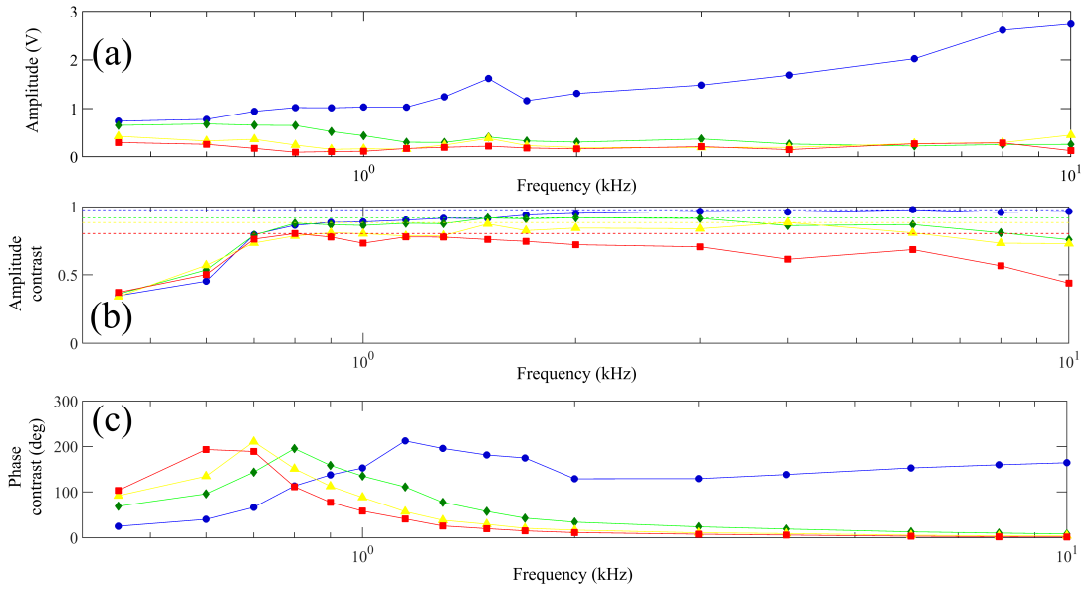

Figure 3. The change in amplitude (**a**–**c**) recorded scanning over an edge of the aluminum plate as a function of the rf primary frequency. The dependence is recorded with the edge covered by zero (blue dots), one (green diamonds), two (yellow triangles) and three (red squares) 0.5 mm-thick aluminium sheets.

The presence of an optimum frequency of operation, i.e., frequency for which there is a maximum change in the signature of the edge (i.e., amplitude, contrast), is easily seen in Figure 3b,c which show the amplitude, C_R, and phase, $C_{Œ}$, contrasts. The amplitude contrast, C_R, is defined in a similar way to [24], $C_R = (R_{Max} - R_{Min})/(R_{Max} + R_{Min})$, and analogously, $C_{Œ} = \phi_{Max} - \phi_{Min}$, with ϕ_{Max}, ϕ_{Min} reflecting the signal phase at the opposite sides of the plate edge. The signal recorded in the immediate vicinity of the edge of the plate is defined by the secondary field produced by the induced eddy currents and the background (i.e., the residual primary field due to imperfect compensation that results from misalignment of the axes). The background value does not show any frequency dependence [30]. For low frequencies, the signal within the plate is dominated by the secondary field, while, outside the plate, it is dominated by the background. At higher frequencies, the increased induction means that the signal from the secondary field is much greater than the background. Hence, the signal inside (before the edge and over the plate), and outside (after the edge and over free space), the plate is dominated by the secondary field. This leads to the saturation of the amplitude contrast C_R that is visible in the blue points in Figure 3b. The dominance of the secondary field in the signal recorded in the vicinity of the edge, both inside and outside of the plate, could also be seen in $C_{Œ}$. The primary rf field produced by the coil along an axis within its cross-section is in the opposite direction to the field created along an axis that lies outside its cross-section, e.g., the opposite direction of field created at either side of a wire. This direction change leads to a 180° change in the phase of the secondary field as the edge of the plate is scanned through the area that is within, to outside, the cross-section of the coil. This change is visible in the value of $C_{Œ}$ for high frequencies, Figure 3c.

The addition of a barrier reduces the amplitude of the edge signature (R), which leads to a reduction in the amplitude (C_R). The optimum frequency depends on the thickness of the barrier. The thicker the barrier, the lower the frequency for which the optimum is observed, i.e., 0.8 kHz for a single 0.5 mm sheet, 0.7 kHz for two, and 0.6 kHz for three sheets.

4.2. Signature of the Recess in the Plate

The results of the tests from the previous section show general properties of the signature of the inhomogeneity but hardly mimics real-life defects. Our next approximation of a defect consists of

a 6 mm-thick aluminium plate containing a 50 mm-diameter recess that is 2.4 mm-deep covered by 0–3 aluminium sheets with 0.5 mm-thickness. Thinning of the plate represents a broad class of defects, ranging from cracks to corrosion. The relatively large recess diameter has been chosen to reduce the effect of the signals produced by the opposite edges of the recess overlapping.

As mentioned before, the amplitude image recorded in the self-compensated configuration represents the measurement of the amplitude components of the secondary field parallel to the surface of the object (plate). For the ideal case, these components have non-zero values only in the immediate vicinity of the edge. Consequently, the amplitude image of the circular recess has a form of a ring profile, Figure 4a, while the phase of the rf signal shows a vortex centred on the recess, Figure 4b [24]. The red dashed line marks the position of the recess edge in Figure 4a,b. As mentioned before, we approximately know the position of the defect, and it has been marked for guides for the eye. The main focus of this work is on the relationship between the defect signature and operating frequency, not on the accurate mapping of the detect. This vortex in the phase image is visible across the whole range of studied frequencies and the following analysis will concentrate only on changes in the amplitude images. We characterise the recess signature similarly to that of the edge. The amplitude of the recess signature is defined as $R = R_{\mathrm{Max}} - R_{\mathrm{Min}}$, with R_{Max}, R_{Min} reflecting signal amplitudes at the top of the profile and in the background of the image. In order to take into account the imperfect compensation of the rf field that introduces inhomogeneities in the measured profile and background amplitudes, we define R_{Max} as an average of the profile amplitude along the circumference of the ring. The value of R_{Min} was calculated as an average of the image background, i.e., average of 10 columns and rows each that make up the edge of the image.

Figure 4 shows the amplitude (c) and amplitude contrast (d) of the profiles representing the recess in the aluminium plate covered by; zero (blue dots), one (green diamonds), and three (red squares) 0.5 mm-thick aluminium sheets; as a function operating frequency. The lift-off between the primary rf coil and the plate with a recess has been kept constant. The frequency dependence of the amplitude, R, of the signatures can be divided into two parts. For the frequencies above 1.5 kHz, the amplitude shows different behaviour depending on the thickness of the barrier. Below this frequency, the behaviour within the three sets of data are similar, which indicates that the dependence is defined by the coupling between the rf field and the plate. As in the previous section, the measured amplitude signature of the uncovered recess increases with frequency, which is a straightforward consequence of the induction law. Consequently, the contrast of the image (C_{R}) with no barriers shows saturation. This saturation occurs at high frequencies (above 4 kHz) since both the signal and the background become defined by the secondary field generated by the surface of the object.

The amplitudes and contrasts of the profiles recorded in the presence of the barrier shows a broad maximum. The frequency for which the maximum contrast is observed depends on the thickness of the barrier (2–3 kHz for 0.5 mm-thick barrier, 1.3–2 kHz for 1.5 mm-thick barrier).

The rf primary field frequency defines the penetration depth of the rf field. The larger the depth, the larger the spatial extent (spread) of the rf primary field within the object is. In turn, the spread of the rf field limits the spatial resolution of the measurement. In this sense, the penetration depth is equivalent to the lift-off, i.e., the distance between the rf primary field coil and the particular layer of the object. Since the image recorded at a particular frequency integrates the contributions from different layers within the object, the total spatial resolution of the measurement is affected by the operational frequency. In particular, for high frequencies, the response from the object will be mostly defined by the contribution from the surface of the object and the resolution of the image will be defined by the size of the coil and step of the scan (about 2 mm). Figure 5 shows the full width at half maximum (FWHM) of the profile in the amplitude image representing the recess as a function of the rf primary field frequency. The profile width values were extracted from the images by fitting two Lorentzian profiles to the cross-section of the image. It is difficult to precisely evaluate the width for frequencies below 1 kHz because of the small profile amplitude. For lift-off values above 5 mm, the width of the profile is defined by the lift-off and does not vary with the rf primary field frequency. We have

recorded images of recesses with three different diameters (50 mm, 25 mm, 12.5 mm) and confirmed that the maximum contrast level decreases with decreasing recess diameter [23].

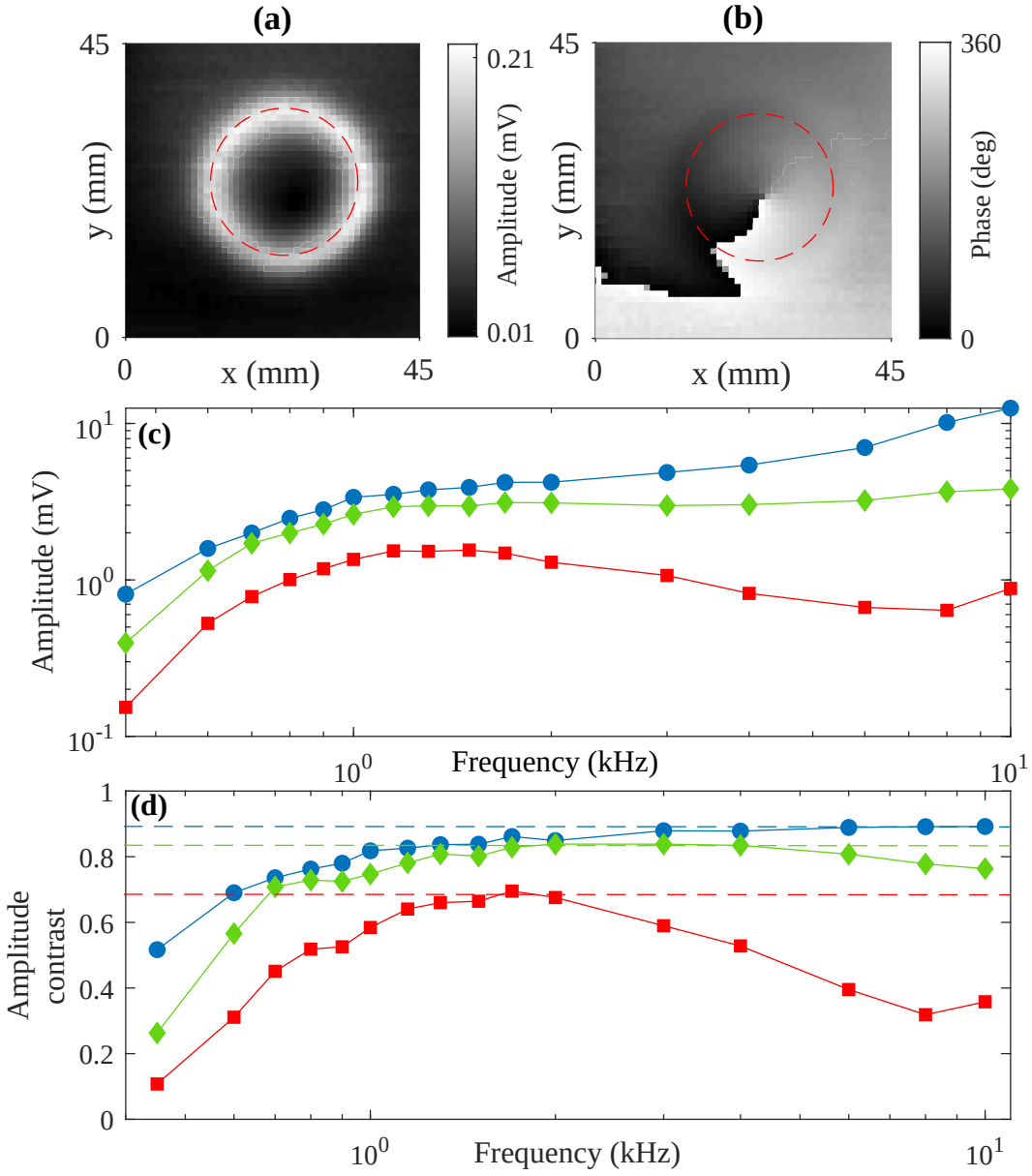

Figure 4. The measured change of the amplitude (**a**) and phase (**b**) of the rf spectroscopy signal recorded in the self-compensation configuration over a 90 × 90 mm^2 area of a 6 mm-thick aluminium plate, containing a 50 mm-diameter recess that is 2.4 mm-deep at 2 kHz. The red dashed line marks the position of the recess edge. The amplitude (**c**) and contrast (**d**) of the profile in the amplitude image representing the recess as a function of the rf primary field frequency. The dependence is recorded with the recess covered by zero (blue dots), one (green diamonds), and three (red squares) 0.5 mm-thick aluminium sheets.

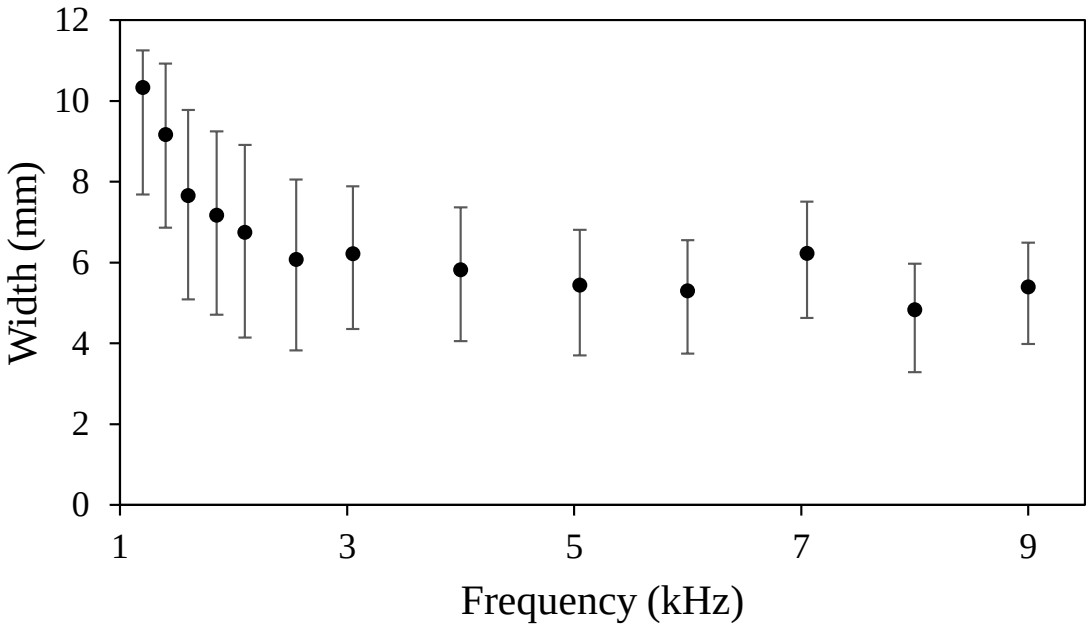

Figure 5. The width (FWHM) of the profiles in the amplitude images representing the recess as a function the rf primary field frequency. The dependence is recorded with the recess covered by a single 0.5 mm aluminium sheet.

At this point, it is worth reminding that the sensitivity of the defect detection with the atomic magnetometer (e.g., C_R) does not only depend on the sensitivity of the sensor but also on its spatial resolution [23]. The latter is defined by the dimensions of the rf primary field coil. For the coil dimensions bigger than these of the defect, the sensor detects a combined signal from opposite sides of the defect. This results in reduced amplitude of the defect signature and difference between observed and actual defect dimensions [23]. In practical implementations, the dimensions of the rf primary field coil are the trade-off between the required spatial resolution, image acquisition rate and the strength of the rf primary field.

4.3. Defect on Inner Wall

Figure 6 shows the amplitude (a)–(d) and phase (e)–(h) images of the aluminium plate containing a recess with variable depth. The plate is flipped such that the recess is on the surface which faces away from the rf coil, i.e., the inner surface [depicted in Figure 2d]. The area of this recess is highlighted by the dashed red square. The signature of this measurement is related to the thickness of the plate, as opposed to the depth of the recess. Within the highlighted area, the thickness of the plate gradually increases from 1 mm at $x = 23$ mm to 6 mm at $x = 64$ mm; and has a constant thickness along $y = 0$ mm to $y = 45$ mm. At the recess edge ($y = 45$ mm), there is a sharp change in thickness to 6 mm. The images are recorded for four values of the operating frequency: 0.6 kHz [(a) and (e)], 1.35 kHz [(b) and (f)], 2.26 kHz [(c) and (g)], and 10 kHz [(d) and (h)]. In contrast to the profiles recorded in the amplitude image where the recess is on the outer surface [shown in Figure 2a], the measured amplitudes produced by the edge and the tilted area of the recess for the inner surface (Figure 6a–d) have a similar value.

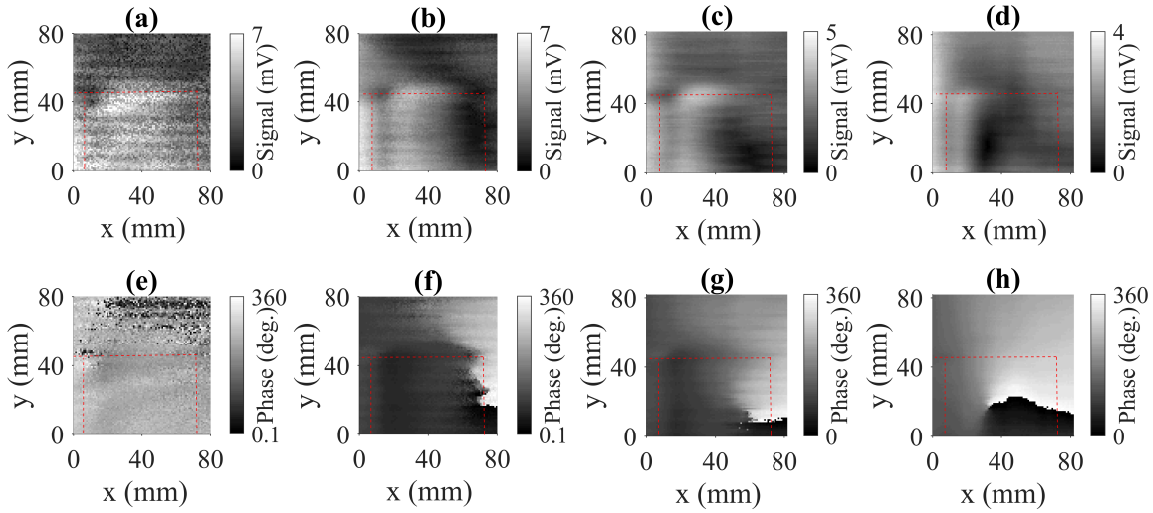

Figure 6. The change of the amplitude (**a**–**d**) and phase (**e**–**h**) of the rf signal recorded for a plate with a continuously changing thickness [shown by Figure 2d] for four values of the rf primary field frequency: (**a**,**e**) 0.6 kHz, (**b**,**f**) 1.35 kHz, (**c**,**g**) 2.26 kHz, (**d**,**h**) 10 kHz. The red dashed line marks a position of the edge of the recess on the under side of the plate. The thickness of the plate gradually increases from 1 mm at $x = 23$ mm to 6 mm at $x = 64$ mm; and has a constant thickness along $y = 0$ mm to $y = 45$ mm.

The change in operating frequency results in a difference in the penetration depth of the primary rf field into the plate. As the frequency is increased, there is a reduction of the extent of the area where the defect signature can be observed in both the amplitude, and the phase images. While the primary rf field penetrates the full depth of the object at low frequencies, which is shown in Figure 6a by the large spatial extent of the recess signature, the contrast of the images recorded at these frequencies is relatively low. This is particularly evident in the degradation of the phase contrast in Figure 6e.

The change of the operating frequency modifies the ratio of the signal components produced by the background and the secondary field. While the amplitude of the background can be assumed to be constant, the amplitude of the secondary field increases with increasing operating frequency. The actual functional frequency dependence of the total secondary field amplitude is a consequence of the fact that the sensor monitors the integrated signal, i.e., the signal produced by different layers of the object. Consequently, the expected linear increase of the secondary field resulting from the induction law is partially compensated by the reduction of the penetration depth of the rf field. The change in the ratio between the components of the signal manifests itself in both the amplitude and phase images.

In the amplitude images, the zero amplitude (black) area visible for the shallow recess depth [Figure 6: (b) $x \approx 70$ mm, (c) $x \approx 60$ mm, and (d) $x \approx 30$ mm], marks the area where the component of the residual primary field that contributes to the background signal and the total secondary field (produced by all layers of the plate) compensate each other. It is worth distinguishing the effects of the secondary field at the outer surface, which is flat, and the inner surface, in the vicinity of the recess. At the outer surface of the plate, the secondary field mostly mirrors the vertical direction of the primary field. A residual component of this is measured since the surface normal of the plate is not exactly parallel with the insensitive axis of the rf magnetometer. The space in the interior of the plate in the immediate vicinity of the recess produces horizontal components of the secondary fields. As the frequency changes, the depth at which the secondary field produced by the interior of the plate compensates the residual primary field will also change due to the change in the optimum coupling between the rf field and the plate. Therefore, the position of this black area occurs at smaller depths for increasing frequency. The change of the ratio between the components of the secondary field generated by the outer and inner surface of the plate is evidenced by the increasing dominance of the vortex in the phase images. When the secondary field from the interior of the plate dominates the signal, the change in phase is small (within the red dashed area in Figure 6 relative to that seen elsewhere in

the image), while, when the phase change of the secondary field from the surface dominates, the phase change is due to the presence of the 360° vortex.

5. Detection of Concealed Defects

The measurement of a series of cavities (holes drilled in the side of an aluminium plate) offset from the surface of the plate at various distances represent the detection of concealed defects, as depicted by the inset in Figure 1. The cavities are 2 mm in diameter and drilled to a length of 40 mm in the side of a 10 mm-thick plate with an area of 140 × 140 mm^2. The cavities run parallel to the surface of the plate. The centre of the holes on one (front) side of the plate are offset by 1.5 mm and 2 mm from the surface, while the holes on the opposite (back) side are offset by 3 mm and 4 mm. The measurement is in the self-compensated configuration, i.e., with the rf primary field coil and the bias field axis orthogonal to the surface of the plate. The geometry of these cavities present no hard edge to the penetrating rf field so it will produce a secondary field with a different spatial distribution to those generated by the circular recesses examined earlier.

Figure 7 shows the amplitude (a) and phase (b) change of the rf atomic magnetometer signal produced by scanning a 165.6 × 165.6 mm^2 area over the plate with cavities. To remove the spatial modulation of the measured amplitude and phase [already discussed in description of Figure 2 and seen prominently in Figure 6a], the images were bandstop filtered (within range 15/pix–25/pix) along the direction parallel to the cavities axis. The plate edges and the positions of the cavities are marked with dotted lines and arrows, respectively. The rf atomic magnetometer was operated at 1.6 kHz. The signatures of all four cavities are visible in both amplitude and phase images. The character of the amplitude of the secondary field in this measurement is similar to that reported in the literature [31]. The signatures of the two holes in the upper part of Figure 7a indicate that, due to the proximity of the plate edge, the compensation of the rf magnetic field is achieved only locally within the area of the defect. Imperfection in rf field compensation is visible as a dark stripe within the defect signature.

Figure 7c shows the dependence of the magnetometer frequency on the amplitude contrast (C_R) while (d) shows the phase contrast, $C_{Œ}$. Consistent with results shown in Figure 4d, the frequency dependence of C_R reaches a broad maximum within 1 kHz–2 kHz range for of the cavities that lie 0.5 mm (blue dots) and 1 mm (green diamonds) under the object surface. The dependencies for cavities that are 2 (yellow triangles) and 3 mm (red squares) deep indicate the presence of a maximum for frequencies below 1 kHz. The spatial extent of the profiles representing the cavity edge is defined by the coil diameter, lift-off distance, operating rf frequency and conductivity of the plate. Since the size of the cavity is comparable to the diameter of the rf primary field coil, the profiles from the opposite edge of the cavities overlap. This overlap results in a reduction of the observed contrast with respect to the values shown in Figure 4d [23]. Imperfections in rf field cancellation are visible in the relatively large variation in the frequency dependence of the phase contrast, $C_{Œ}$. Nevertheless, the general trend mirrors that of the frequency dependence of the amplitude contrast. The advantage of $C_{Œ}$ is the large dynamic range of the defect signatures measured, even for frequencies outside the optimum range, i.e., 1 kHz–2 kHz, where the maximum value of the C_R and $C_{Œ}$ are reached.

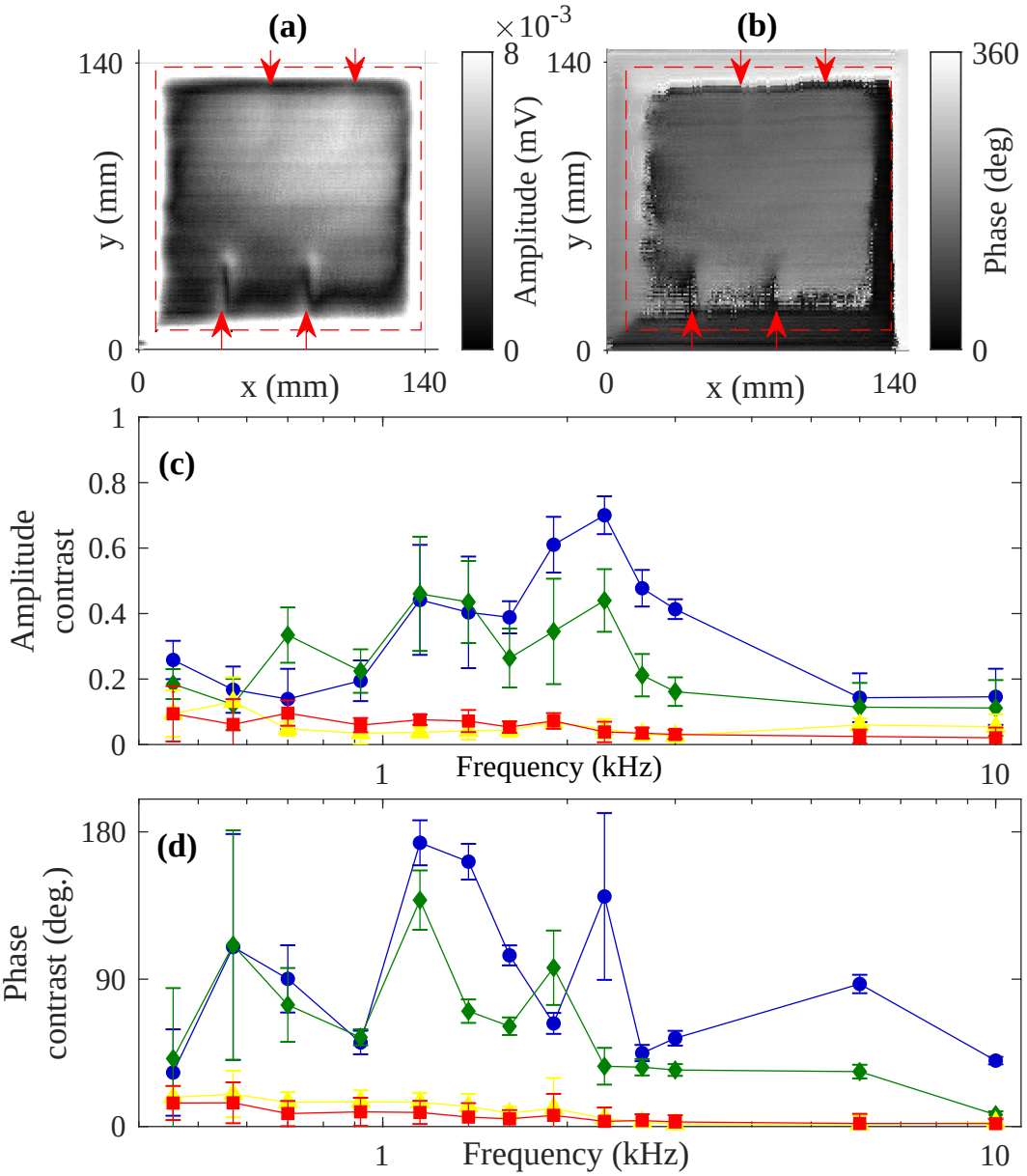

Figure 7. (**a**) amplitude and (**b**) phase change in the rf atomic magnetometer signal generated by scanning a 165.6 × 165.6 mm^2 area over a square 140 × 140 mm^2 aluminium plate with cavities that are 2 mm in diameter and are drilled to a length of 40 mm in the side of the plate. Plate edges are marked by dashed lines while the position of the holes is indicated by the arrows. Plots of the frequency dependence of the amplitude, C_R, (**c**) and phase, C_{CE}, (**d**) contrast of the 0.5 mm (blue dots), 1 mm (green diamonds), 2 mm (yellow triangles), and 3 mm (red squares) deep cavities with changing frequency.

6. Conclusions

We have presented the results of a series of NDT measurements with an rf atomic magnetometer involving various types of concealed defects. In particular, we have studied the shape and frequency dependence of signatures of the defects that are represented by the edge of a plate, a recess and cavities in an aluminium plate. We have experimentally explored the optimum operational frequency, which addresses the issue of the coupling between the rf primary field and the investigated object. We have achieved consistency across different measurement types. The optimum in the frequency

dependence of the amplitude/phase contrast for defects under a 0.5 mm–1.5 mm conductive barrier was observed within the 1 kHz–2 kHz frequency range. It is worth pointing out that these values are significantly higher than those reported in [32] in the context of measurements with pick up coils, where the maximum in the defect signature has been observed between 5 Hz and 10 Hz. The optimum frequency for a given penetration depth is defined by the coupling between the rf field and the object. The optimum is a balance between the induced field strength and the skin depth, which are respectively proportional and inversely proportional to the operating frequency for the rf field. This balance implicitly includes the performance of the sensor, which for increased sensitivities will be able to detect a lower signal produced by a defect over a higher frequency range. In our opinion, this explains the shift of the optimum frequency range presented in this paper with respect to that described in [32]. Further improvements in the sensitivity of the rf atomic magnetometer should allow operation of a concealed defect detection system at even higher frequencies, which would be beneficial for operation in industrial environments where there are low-frequency environmental noises.

Author Contributions: Conceptualization, W.C. and R.G.; methodology, W.C., R.G., and P.B.; software, R.G. and P.B.; validation, R.G. and P.B.; formal analysis, R.G. and P.B.; writing—original draft preparation, W.C.; writing—review and editing, W.C., R.G., and P.B.; supervision, W.C.; project administration, W.C.; funding acquisition, W.C. All authors have read and agreed to the published version of the manuscript.

Funding: The work was funded by the UK Department for Business, Energy and Industrial Strategy. P.B. was supported by the Engineering and Physical Sciences Research Council (EPSRC) (No. EP/P51066X/1).

Conflicts of Interest: The authors declare no conflict of interest.

References

1. Maldague, X.P. Introduction to NDT by active infrared termography. *Mater. Eval.* **2002**, *60*, 1060–1073.
2. Vavilov, V.P.; Burleigh, D.D. Review of pulsed thermal NDT: Physical principles, theory and data processing. *NDT E Int.* **2015**, *73*, 28. [CrossRef]
3. Maldague, X.P.V. *Theory and Practice of Infrared Technology for Nondestructive Testing*; Wiley-Interscience: New York, NY, USA, 2001.
4. Felice, M.V.; Velichko, A.; Wilcox, P.D. Accurate depth measurement of small surface-breaking cracks using an ultrasonic array post-processing technique *NDT E Int.* **2014**, *68*, 105–112. [CrossRef]
5. Hellier, C. *Handbook of Nondestructive Evaluation*; Mcgraw-Hill: New York, NY, USA, 2001.
6. Griffiths, H. Magnetic induction tomography. *Meas. Sci. Technol.* **2001**, *12*, 1126–1131. [CrossRef]
7. Auld, B.A.; Moulder, J.C. Review of advances in quantitative eddy current nondestructive evaluation. *J. Nondestr. Eval.* **1999**, *18*, 3–36. [CrossRef]
8. Perez, L.; le Hir, J.; Dolabdjian, C.; Butin, L. Ivestigation in detection of fatigue cracks under rivet head airframe using improved gmr magnetometer in an eddy current system. *J. Electr. Eng.* **2004**, *55*, 73–76.
9. Sophian, A.; Tian, G.; Fan, M. Pulsed eddy current non-destructive testing and evaluation: A review. *Chin. J. Mech. Eng.* **2017**, *30*, 500. [CrossRef]
10. Ma, L.; Soleimani, M. Magnetic induction tomography methods and applications: A review. *Meas. Sci. Technol.* **2017**, *28*, 072001–072012. [CrossRef]
11. Savukov, I.M.; Seltzer, S.J.; Romalis, M.V. Detection of NMR signals with a radio-frequency atomic magnetometer. *J. Magn. Res.* **2007**, *185*, 214–220. [CrossRef] [PubMed]
12. Dogaru, T.; Smith, S.T. Edge crack detection using a giant magnetoresistance based eddy current sensor. *Nondestruct. Test. Eval.* **2000**, *16*, 31–53. [CrossRef]
13. Dogaru, T.; Smith, S.T. Giant magnetoresistance-based eddy-current sensor. *IEEE Trans. Magn.* **2001**, *37*, 3831–3838. [CrossRef]
14. Ripka, P.; Janosek, M. Advances in magnetic field sensors. *IEEE Sens. J.* **2010**, *10*, 1108–1116. [CrossRef]
15. Krause, H.J.; Kreutzbruck, M.V. Recent developments in SQUID NDE. *Phys. C* **2002**, *368*, 70–79. [CrossRef]
16. Storm, J.; Hömmen, P.; Drung, D.; Körber, R. An ultra-sensitive and wideband magnetometer based on a superconducting quantum interference device. *Appl. Phys. Lett.* **2017**, *110*, 072603. [CrossRef]
17. Deans, C.; Marmugi, L.; Hussain, S.; Renzoni, F. Electromagnetic induction imaging with a radio-frequency atomic magnetometer. *Appl. Phys. Lett.* **2016**, *108*, 103503. [CrossRef]

18. Wickenbrock, A.; Leefer, N.; Blanchard, J.W.; Budker, D. Eddy current imaging with an atomic radio-frequency magnetometer. *Appl. Phys. Lett.* **2016**, *108*, 183507. [CrossRef]
19. Deans, C.; Marmugi, L.; Renzoni, F. Through-barrier electromagnetic imaging with an atomic magnetometer. *Opt. Exp.* **2017**, *25*, 17911–17917. [CrossRef]
20. Deans, C.; Marmugi, L.; Renzoni, F. Sub-picotesla widely tunable atomic magnetometer operating at room-temperature in unshielded environments. *Rev. Sci. Instrum.* **2018**, *89*, 083111. [CrossRef]
21. Deans, C.; Marmugi, L.; Renzoni, F. Active underwater detection with an array of atomic magnetometers. *Appl. Opt.* **2018**, *57*, 2346–2351. [CrossRef]
22. Bevington, P.; Gartman, R.; Chalupczak, W.; Deans, C.; Marmugi, L.; Renzoni, F. Non-destructive structural imaging of steelwork with atomic magnetometers. *App. Phys. Lett.* **2018**, *113*, 063503. [CrossRef]
23. Bevington, P.; Gartman, R.; Chalupczak, W. Imaging of material defects with a radio-frequency atomic magnetometer. *Rev. Sci. Instrum.* **2019**, *90*, 013103. [CrossRef] [PubMed]
24. Bevington, P.; Gartman, R.; Chalupczak, W. Enhanced material defect imaging with a radio-frequency atomic magnetometer. *J. Appl. Phys.* **2019**, *125*, 094503. [CrossRef]
25. Bevington, P.; Gartman, R.; Chalupczak, W. Alkali-metal spin maser for non-destructive tests. *App. Phys. Lett.* **2019**, *115*, 173502. [CrossRef]
26. Bevington, P.; Gartman, R.; Chalupczak, W. Magnetic induction tomography of structural defects with alkali-metal spin maser. *Appl. Opt.* **2020**, *59*, 2276. [CrossRef] [PubMed]
27. Chalupczak, W.; Godun, R.M.; Pustelny, S.; Gawlik, W. Room temperature femtotesla radio-frequency atomic magnetometer. *Appl. Phys. Lett.* **2012**, *100*, 242401. [CrossRef]
28. Takahashi, Y.; Honda, K.; Tanaka, N.; Toyoda, K.; Ishikawa, K.; Yabuzaki, T. Quantum nondemolition measurement of spin via the paramagnetic Faraday rotation. *Phys. Rev. A* **1999**, *60*, 4974–4979. [CrossRef]
29. Savukov, M.; Seltzer, S.J.; Romalis, M.V.; Sauer, K.L. Tunable atomic magnetometer for detection of radio-frequency magnetic fields. *Phys. Rev. Lett.* **2005**, *95*, 063004. [CrossRef] [PubMed]
30. Gruber, B.; Froeling, M.; Leiner, T.; Klomp, D.W.J. RF coils: A practical guide for nonphysicists. *J. Magn. Reson. Imaging* **2018**, *48*, 590-604. [CrossRef] [PubMed]
31. Hesse, O.; Pankratyev, S. Usage of Magnetic Field Sensors for Low Frequency Eddy Current Testing. *Meas. Sci. Rev.* **2005**, *5*, 86.
32. Yoshimura, W.; Sasayama, T.; Enpuku, K. Optimal Frequency of Low-Frequency Eddy-Current Testing for Detecting Defects on the Backside of Thick Steel Plates. *IEEE Trans. Magn.* **2019**, *55*, 8645817. [CrossRef]